GPS measurements of current crustal movements along the Dead Sea Fault

S. Wdowinski,[1,2] Y. Bock,[3] G. Baer,[4] L. Prawirodirdjo,[3] N. Bechor,[1] S. Naaman,[1] R. Knafo,[4] Y. Forrai,[5] and Y. Melzer[5]

Received 19 June 2003; revised 25 November 2003; accepted 10 December 2003; published 11 May 2004.

[1] A network of 11 continuous GPS stations was constructed in Israel between 1996 and 2001 to monitor current crustal movements across the Dead Sea Fault (DSF). Analysis of the GPS measurements with respect to the ITRF2000 Reference Frame yields time series of daily site positions containing both secular and seasonal variations. Horizontal secular variations (station velocities) are evaluated with respect to the main tectonic element in the region, the DSF. We use six velocity vectors west of the DSF to define the ITRF2000 pole of the Sinai sub-plate, and rotate the velocity field for all stations into the Sinai reference frame (SRF). The velocity vectors reveal that (1) relative station movements are less than 4 mm/yr; (2) the nine stations located west of the DSF show no statistically significant motion with respect to the SRF; and (3) the two stations located in the Golan Heights (KATZ and ELRO) and a station in Damascus, Syria (UDMC) show 1.7–2.8 mm/yr northward motion with respect to Sinai, indicating a left-lateral motion along the DSF. Using locked-fault models, we estimate the current slip rate across the DSF as 3.3 ± 0.4 mm/yr. If we exclude the northern sites (ELRO and UDMC), which are located adjacent to the compressional jog of Mount Hermon, our estimate increases to 3.7 ± 0.4 mm/yr. The calculated ITRF2000 Sinai, Eurasia, and Nubia poles and a published pole for Arabia allow us to calculate the current relative plate motion of Sinai-Arabia and Sinai-Nubia. *INDEX TERMS:* 1206 Geodesy and Gravity: Crustal movements—interplate (8155); 1242 Geodesy and Gravity: Seismic deformations (7205); 8150 Tectonophysics: Plate boundary—general (3040); 8158 Tectonophysics: Plate motions—present and recent (3040); *KEYWORDS:* Dead Sea Fault, space geodesy, eastern Mediterranean

Citation: Wdowinski, S., Y. Bock, G. Baer, L. Prawirodirdjo, N. Bechor, S. Naaman, R. Knafo, Y. Forrai, and Y. Melzer (2004), GPS measurements of current crustal movements along the Dead Sea Fault, *J. Geophys. Res.*, *109*, B05403, doi:10.1029/2003JB002640.

1. Introduction

[2] Owing to its unique tectonic setting as a continental transform plate boundary, the Dead Sea Fault (DSF) has been intensively studied. *Wilson* [1965], who introduced the concept of transform faults, suggested that the DSF serves as a transform plate boundary between Nubia and Arabia. *McKenzie et al.* [1970] and *Freund* [1970] noted that the orientation of the DSF does not follow the expected direction of a transform fault between Nubia and Arabia (small circle about their pole). They postulated the existence of the Sinai sub-plate, which partitions divergent Arabia-Nubia motion along the Red Sea into transcurrent motion along the DSF and divergence across the Gulf of Suez (Figure 1, insert).

[3] The relative motion across the DSF has been estimated both by regional plate motion models and local slip rate (displacement divided by time) considerations. So far, global plate motion models have ignored the Sinai sub-plate due to the lack of standard geological constraints (marine magnetic anomalies, transform fault orientation, slip vectors) along the sub-plate boundary. The regional plate motion studies use the fault orientation, additional local observations, and constraints from the motion of neighboring plates to estimate 5–10 mm/yr of relative motion across the DSF [*Le Pichon and Francheteau*, 1978; *Garfunkel*, 1981; *Joffe and Garfunkel*, 1987; *Chu and Gordon*, 1998]. Local geologic and seismic studies, which estimate the slip rate across the DSF, yield a wider range of relative motion estimates, from 1 to 10 mm/yr [e.g., *Quennell*, 1959; *Freund et al.*, 1970; *McKenzie et al.*, 1970; *Le Pichon and Fancheteau*, 1978; *Ben-Avraham et al.*, 1979; *Ben-Menahem and Aboodi*, 1981; *Garfunkel*, 1981; *Joffe and Garfunkel*, 1987; *Salamon*, 1993; *Shapira and*

[1]Department of Geophysics and Planetary Sciences, Raymond and Beverly Sackler Faculty of Exact Sciences, Tel Aviv University, Ramat Aviv, Israel.
[2]Also at Division of Marine Geology and Geophysics, Rosenstiel School of Marine and Atmospheric Science, University of Miami, Miami, Florida, USA.
[3]Cecil H. and Ida M. Green Institute of Geophysics and Planetary Physics, Scripps Institution of Oceanography, La Jolla, California, USA.
[4]Geological Survey of Israel, Jerusalem, Israel.
[5]Survey of Israel, Tel Aviv, Israel.

0148-0227/04/2003JB002640$09.00

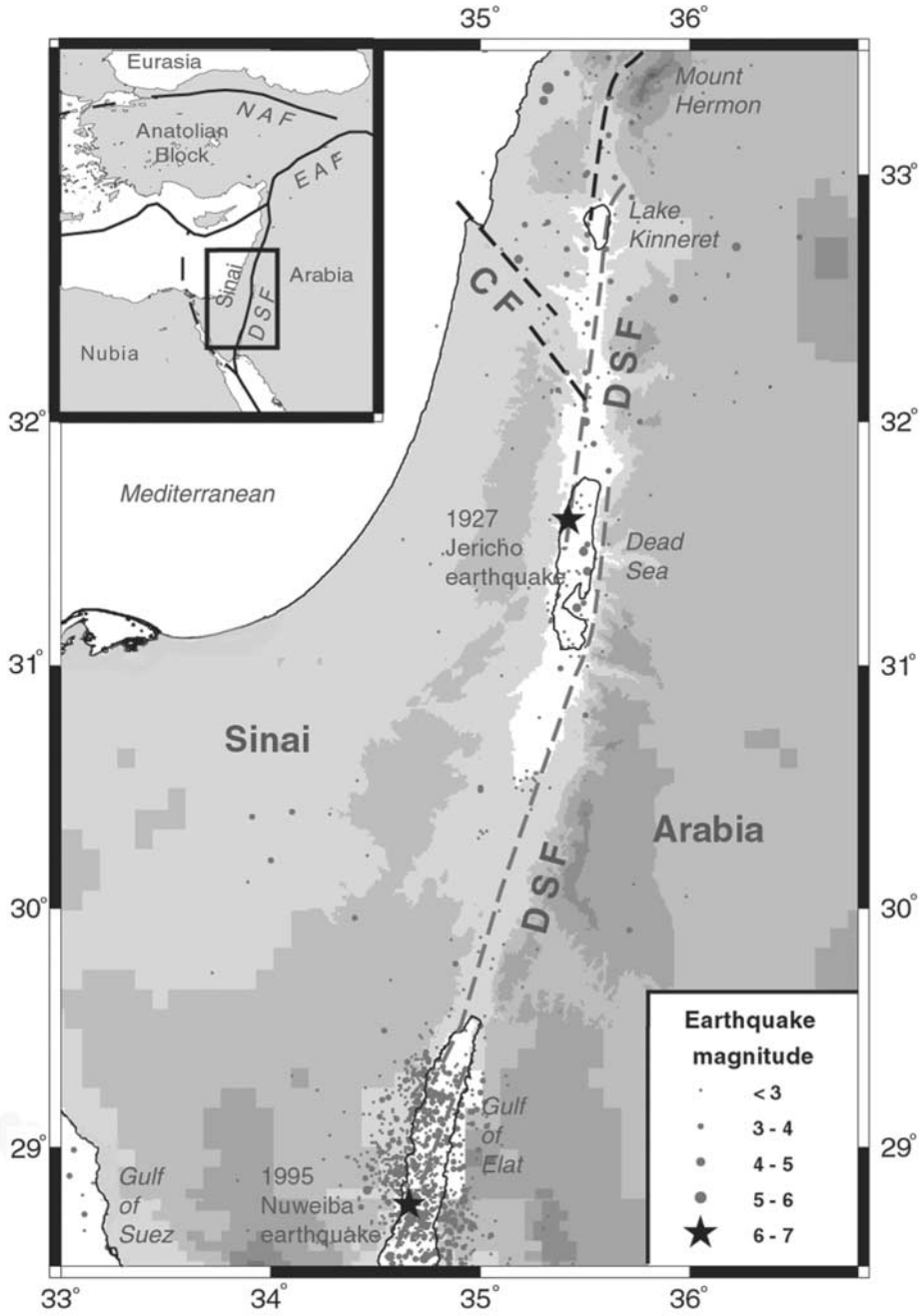

Figure 1. Location map of the Southern Levant showing the overall geography of the region, main tectonic elements, and earthquake epicenters [*Geophysical Institute of Israel*, 1996]. Insert is location map of the eastern Mediterranean region showing the tectonic plates and their boundaries. Abbreviations: CF, Carmel Fault; DSF, Dead Sea Fault; EAF, East Anatolian Fault; NAF, North Anatolian Fault.

Hofstetter, 1993; *Enzel et al.*, 1994; *Ginat et al.*, 1998; *Klinger et al.*, 2000a, 2000b]. Generally, seismic estimates show a rate of only 1–4 mm/yr, geomorphologic estimates are in the range of 3–7 mm/yr, whereas long-term geological estimates are in the range of 6–10 mm/yr.

[4] Space geodetic technologies, in particular GPS, provided the first direct estimates of current plate motion in the eastern Mediterranean. Early studies, which used episodic measurements, were able to detect the relative plate motion between Sinai, Nubia, and Eurasia [*Smith et al.*, 1994; *Bechor and Wdowinski*, 1998; *McClusky et al.*, 2000; *McClusky et al.*, 2003]. Owing to the low rates of crustal movements in the region, episodic measurements were not accurate enough to detect interseismic deformation across the DSF [*Adler et al.*, 2001; *Ostrovsky*, 2001; *Even-Tzur*, 2001]. Coseismic deformation induced by the M = 7.2 1995 Nuweiba earthquake was detected by episodic GPS measurements [*Kimata et al.*, 1997; *Bechor*, 1998], as well

as by InSAR [*Baer et al.*, 1999, 2001]. On the basis of three-dimensional elastic earthquake modeling of the InSAR observed deformation, *Shamir et al.* [2003] estimated that the geodetic moment release accounted for 90% of the seismic moment release.

[5] In this study we use continuous GPS (CGPS) observations measured on both sides of the DSF to calculate the spatial distribution of crustal deformation and the current tectonic plate motion in the eastern Mediterranean. Observations were collected from 1996 to 2002 by 11 CGPS stations of the GIL (GPS in Israel) network [*Wdowinski et al.*, 2001] and two additional stations, Amman, Jordan, and Damascus, Syria (Figure 2). The geographic distribution of the CGPS stations defines our study area to the southern two thirds of the DSF, from Mount Hermon in the north to the Gulf of Elat in the south (Figure 2). Thus our usage of DSF throughout this study refers to the southern two thirds of the DSF only. This study expands upon initial results published by *Pe'eri et al.* [2002], who used 3 years of data from the first three CGPS stations in Israel to estimate the current slip rate across the DSF, at 2.6 ± 1 mm/yr. Our current analysis is based on a larger network, longer time span, and improved modeling. It also enables us to calculate the poles and rates of the relative plate motion between Sinai and Arabia, Eurasia, and Nubia.

2. Tectonic Setting

[6] The DSF is a transform plate boundary separating the Arabian plate from the Sinai sub-plate. It transforms the Arabia-Nubia divergent motion in the Red Sea into the convergence motion between Eurasia and Arabia, currently expressed by extrusion of Anatolia (Figure 1, insert). However, not all the African-Arabian divergent motion is transferred northward to the convergence zones. Some of the divergent motion in the Red Sea propagates into the Gulf of Suez, which forms the southwestern boundary between Nubia and Sinai. North of the Gulf, the Nubia-Sinai boundary is diffuse and hard to locate. Additional divergent motion is taken up by secondary faults branching off the main trace of the DSF north of the Dead Sea (Figure 1). The activity along the DSF has been continuous since the Miocene to the present [*Quennell*, 1959; *Garfunkel*, 1981, 1988; *Garfunkel et al.*, 1981; *Heimann*, 1990; *Belitzki*, 1997; *Marco et al.*, 1997; *Ellenblum et al.*, 1998]. The total displacement across the southern section of the DSF (south of 32°N) was estimated as 105 km [*Quennell*, 1958; *Freund et al.*, 1968], whereas across the northern section the estimated displacement is significantly less [*Dubertret*, 1962; *Garfunkel*, 1981].

[7] The DSF is subjected to a moderate level of seismicity (Figure 1). The highest recorded seismic activity was in the Gulf of Elat (Aqaba), the location of the 1995 Nuweiba earthquake [*Shamir*, 1996; *Pinar and Turkelli*, 1997; *Baer et al.*, 1999; *Klinger et al.*, 1999; *Hofstetter*, 2003; *Hofstetter et al.*, 2003; *Shamir et al.*, 2003]. Another area of concentrated activity is the area of the Dead Sea, where the M = 6.5, 1927 Jericho earthquake occurred [*Avni et al.*, 2002]. Seismic activity along the Arava Valley, which is located between the Gulf of Elat (Aqaba) and the Dead Sea, is very limited. North of the Dead Sea, seismic activity is distributed over a wide area, reflecting diffuse deformation in northern Israel and Lebanon. On the basis of the earthquake distribution in the region, *Salamon et al.* [1996] suggested that the Carmel Fault represents the northern extent of the Sinai sub-plate.

3. GIL Network

[8] The GIL network consists of 11 CGPS stations (Figure 2, Table 1). The network provides a reference frame for precise GPS measurements in Israel, and serves basic and applied geophysical research. The GIL network also provides CGPS data to the International GPS Service (IGS) for calculating precise orbits and Earth orientation parameters (EOP). RAMO is the official IGS station in Israel. It is located in the central Negev, about 50 km from the DSF, and therefore considered to be tectonically stable.

[9] The network includes four stations with geodetic monuments installed on roofs of buildings between 1996 and 1998 by the Survey of Israel (SOI), mainly for geodetic purposes. The other seven stations have very stable monuments [*Knafo and Wdowinski*, 2000] that were constructed since 1998, with an emphasis on geophysical research, by a joint team of scientists from Tel Aviv University (TAU), Scripps Institution of Oceanography (SIO), the Survey of Israel (SOI), and the Geological Survey of Israel (GSI). The actual locations were determined according to bedrock exposure, undisturbed view of the sky for clear signal reception, and logistical factors including power and telephone connections and protection from vandalism. Each station is equipped with a geodetic GPS receiver (Trimble SSE or Ashtech Z-12), geodetic antenna (L1/L2 antenna for Trimble receivers and Dorne-Margolin antenna with choke rings for Ashtech receivers), AC power, emergency backup power, a dedicated telephone line, and a modem (Table 1). The antenna is mounted on the monument, whereas the rest of the equipment is stored in a specially designed metal box. Data collection is at 24-hour intervals (0000-2400 UT) using a 30-s receiver-sampling rate. The data collection and processing center at TAU downloaded the data described in this paper once a day, using automated procedures. The data download and archiving tasks have been recently transferred to the Survey of Israel. Historical and current data are available at the SOPAC archive (anonymous ftp://garner.ucsd.edu). *Knafo and Wdowinski* [2000] and *Wdowinski et al.* [2001] provide more detailed descriptions of the GIL network.

[10] In addition to the GIL network, CGPS observations were also collected in Amman, Jordan (AMMN in Figure 2), by the Royal Jordanian Geographic Centre (RJGC) and in Damascus, Syria (UDMC in Figure 2). The two stations are the only regional stations located significantly east of the DSF. The AMMN station, which is the official Jordanian IGS station, was built by the RJGC with assistance from SIO. It operated continuously from mid-1999 to mid-2002 with a 30-s receiver sampling rate with data pushed daily to the SOPAC archive. Unfortunately, our analysis of the data indicated that the site exhibited significant unexplained motions during this period

4. GPS Data Processing and Results

[11] The GPS observations were processed in a three-step procedure using the GAMIT/GLOBK software packages,

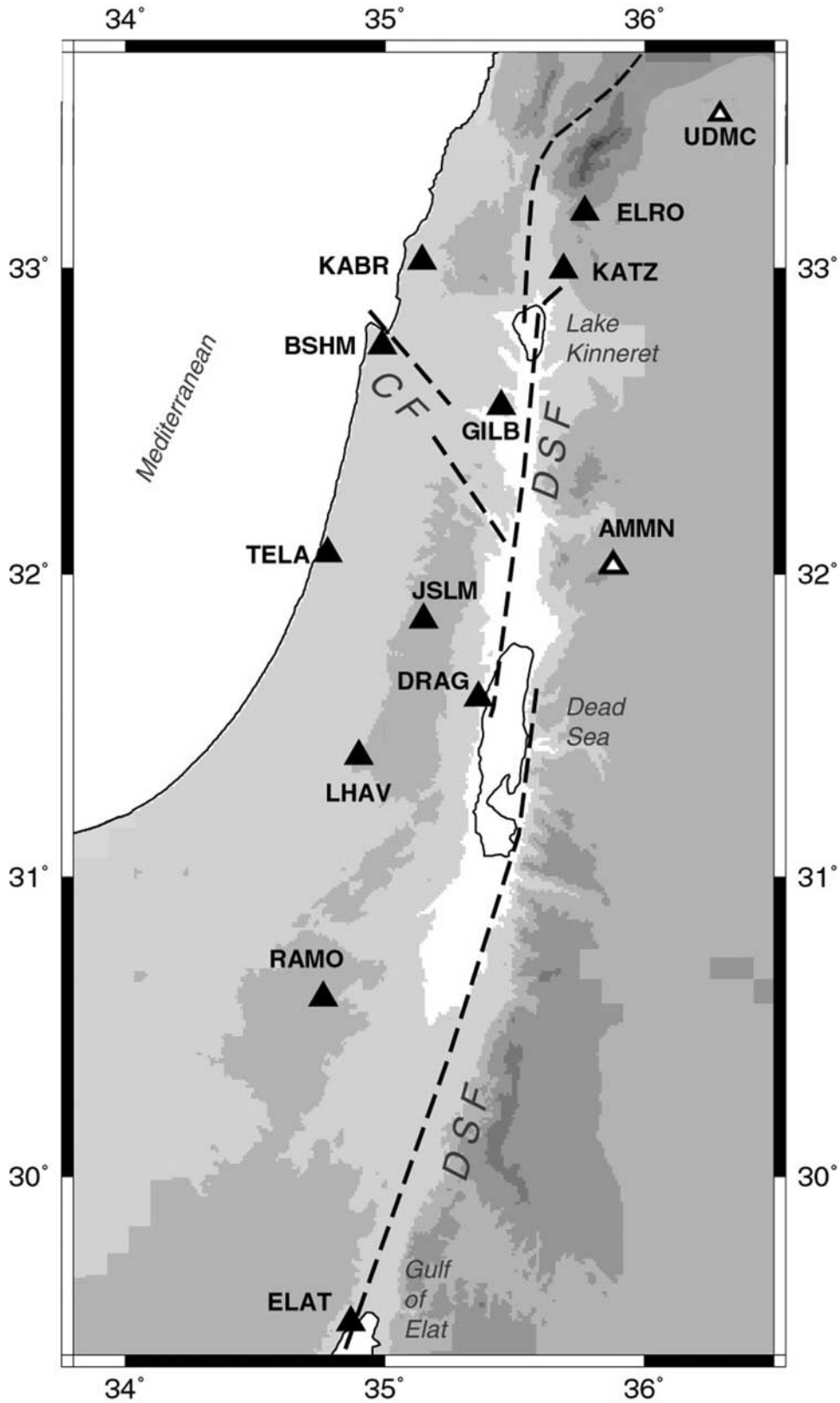

Figure 2. Geographic location of the GIL (solid triangles), AMMN and UDMC (open triangles) permanent GPS stations and main tectonic elements in the southern Levant. Abbreviations: CF, Carmel Fault; DSF, Dead Sea Fault.

Table 1. GIL/AMMN/UDMC Site Metadata

Site Code	Site Name and Location	Geodetic Coordinates	Equipment Type (Receiver/Antenna)	Monument Description	Start Date, YY.DDD
AMMN	Royal Jordanian Geographic Centre HQ, Amman	32.01°N 35.88°E 1055.8 m	Ashtech Z-XII3/ ASH700936D_M	metal adaptor mounted to a concrete pillar (boarder-stone)	1999.237
BSHM	Haifa, The Binyamin Shmuter Memorial Station	32.78°N 35.02°E 225.1 m	Ashtech Z-XII3/ ASH700228D	stainless steel pin attached to the roof of a stable building	1998.245
DRAG	Metzokey Dragot, Dead Sea	31.59°N 35.39°E 120.3 m	Ashtech Z-XII3/ ASH700936D_M Choke-ring	stainless steel rod inserted into a concrete block	2000.038
ELAT[a]	Elat	29.51°N 34.92°E 29.6 m	Trimble 4000SSE/ Trimble 4000ST L1/L2 GEOD	stainless steel pin attached to the roof of a stable building	1997.040
ELRO	Kibbutz Elrom, Golan Heights	33.18°N 35.77°E 1080.4 m	Ashtech Z-XII3/ ASH700936D_M Choke-ring	stainless steel rod inserted into a concrete block	2000.101
GILB	Kibbutz Ma'ale Gilbo'a, Mount Gilbo'a	32.48°N 35.42°E 525.4 m	Ashtech Z-XII3/ ASH700936D_M Choke-ring	stainless steel rod in bedrock outcropping	1998.212
JSLM	Jerusalem	31.76°N 35.20°E 814.6 m	Ashtech Z-XII3/ ASH701945B_M Choke-ring	stainless steel rod in bedrock outcropping	2001.171
KABR	Kibbutz Kabri, Western Galilee	33.02°N 35.14°E 119.4 m	Ashtech Z-XII3/ ASH700936D_M Choke-ring	a shallow braced monument with 4-m anchor	1998.205
KATZ[a]	Katzerin, Golan Heights	33.00°N 35.69°E 347.0 m	Trimble 4000SSE/ Trimble 4000ST L1/L2 GEOD	stainless steel pin attached to the roof of a stable building	1996.217
LHAV	Kibbutz Lahav, Northern Negev	31.38°N 34.87°E 488.9 m	Ashtech Z-XII3/ ASH701945B_M Choke-ring	a shallow braced monument with 4-m anchor	2001.012
RAMO	Mitzpe Ramon, The Tel Aviv University Wise Astronomical Observ.	30.60°N 34.76°E 893.1 m	Ashtech Z-XII3/ ASH700936D_M Choke-ring	stainless steel rod in bedrock outcropping	1998.162
TELA[a]	Tel Aviv	32.07°N 34.78°E 58.4 m	Trimble 4000SSE/ Trimble 4000ST L1/L2 GEOD	stainless steel pin attached to the roof of a stable building	1996.217
UDMC	Damascus	33.31°N 36.17°E 1064 m	Ashtech Z-XII3/ ASH700936B_M Choke-ring		2001.143

[a]Equipment at ELAT, KATZ, and TELA was replaced in March 2003 with Ashtech receivers, and at TELA also with Ashtech choke-ring antenna.

version 10.06 [*King and Bock*, 2000; *Herring*, 2000]. In the first step, we used the GAMIT software with loose constraints to analyze daily CGPS data of the global IGS network, consisting of 80–120 stations, in order to calculate precise orbits and EOP. In the second stage, we also used GAMIT and the calculated orbits and EOP to process with tight constraints daily CGPS data of the GIL stations and the 10–12 nearest IGS stations (Figure 3), solving for daily three-dimensional station positions. In the third stage, we used the GLOBK software to analyze all global and regional solutions day-by-day to align all calculated station positions into the ITRF2000 reference frame [*Altamimi et al.*, 2002].

[12] The final product of the GAMIT/GLOBK analyses is a three-component time series of daily station positions with respect to ITRF2000. By applying a spatial filtering analysis [*Wdowinski et al.*, 1997], we improve signal-to-noise ratio of the time series, thereby improving the accuracy of our modeled parameters (e.g., rates and seasonal terms). The filtered series are shifted from the original ITRF2000 reference frame (RF) and, hence, are no longer represented in the global RF [*Wdowinski et al.*, 1997]. Because the regional offset from the RF is very small, we term the new RF as ITRF2000*.

[13] Figure 4 presents the filtered GIL/AMMN time series, with respect to the average three-dimensional (N, E, U) ITRF2000* location of each station. The longest time series are KATZ and TELA, which began operation in 1996. Some stations are missing subsets of the data due to technical and/or logistical problems. At three stations (GILB, KABR, and RAMO), we changed antennas during 2001 (vertical lines in Figure 4) due to a recall by the manufacturer. Unfortunately, the replaced antenna of RAMO had a hardware problem, resulting in very noisy data. Additional equipment change occurred in BSHM (antenna replacement in 2001), ELAT and KATZ (receiver replacement in 2003), and TELA (receiver and antenna replacement in 2003).

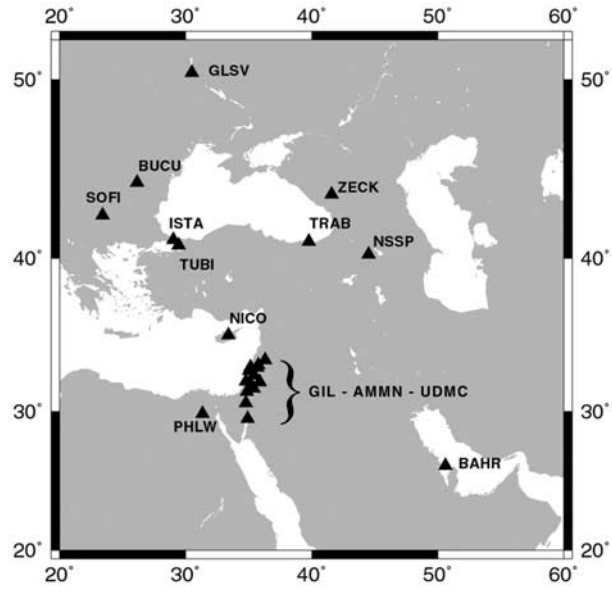

Figure 3. Geographic distribution of the 10 IGS and the 13 GIL/AMMN/UDMC stations used in Eastern Mediterranean regional data processing analysis.

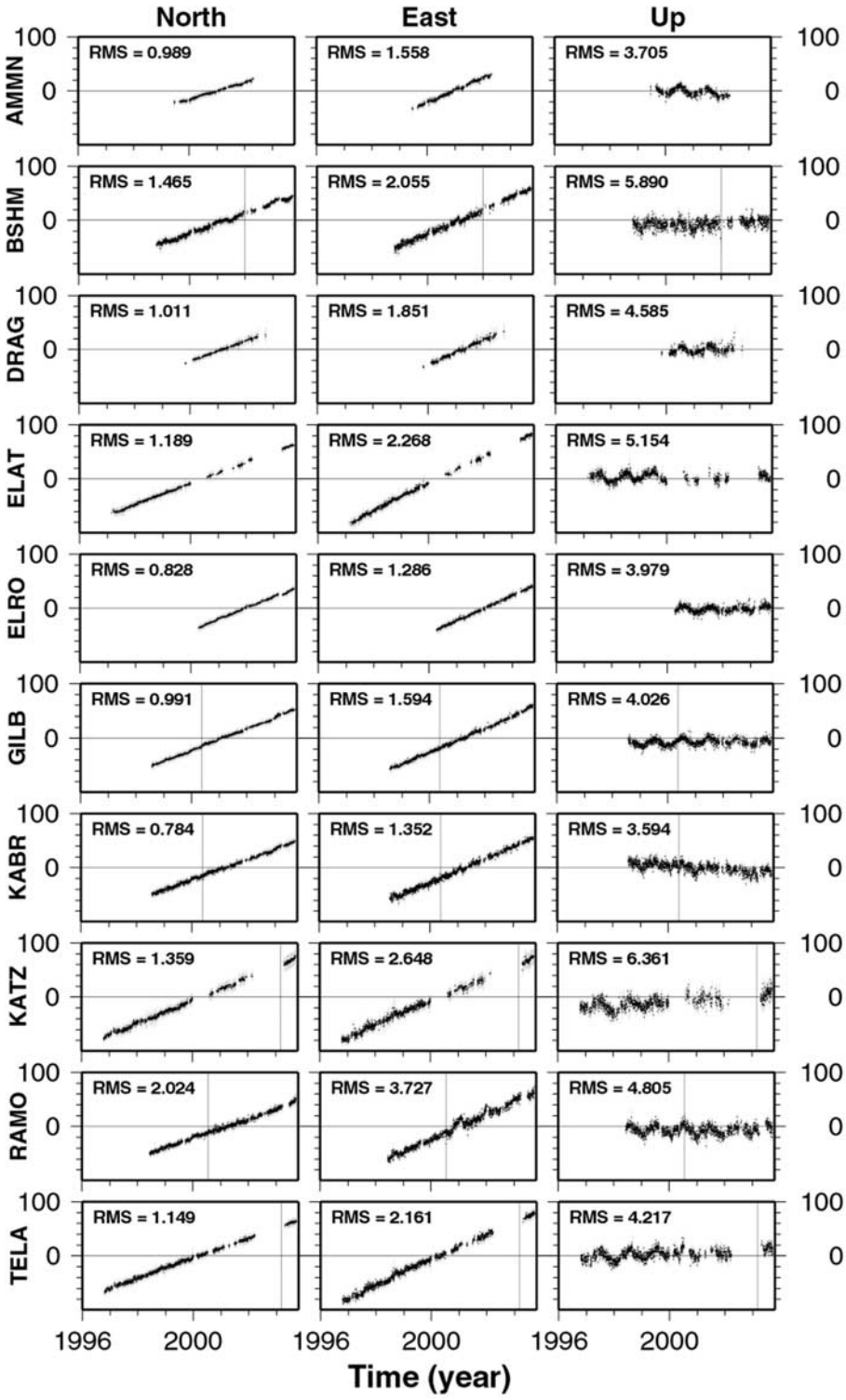

Figure 4. Time series of the filtered GIL/AMMN station positions (mm) with respect to ITRF2000* (spatially filtered ITRF2000 reference frame). Daily relative positions (with respect to an average value) are marked by black dots, and their 1-σ uncertainties are shown by shaded error bars. Vertical lines mark the date of antenna and/or change.

[14] The time series show two dominant patterns of position changes with time: secular (linear) and seasonal (sinusoidal) (Figure 4); seasonal position variations represent both annual and semi-annual periods [*Dong et al.*, 2002; *Nikolaidis*, 2002]. The secular position change is dominant in the horizontal components, whereas the seasonal is dominant in the vertical one. The horizontal time series exhibit the combined effect of the two patterns,

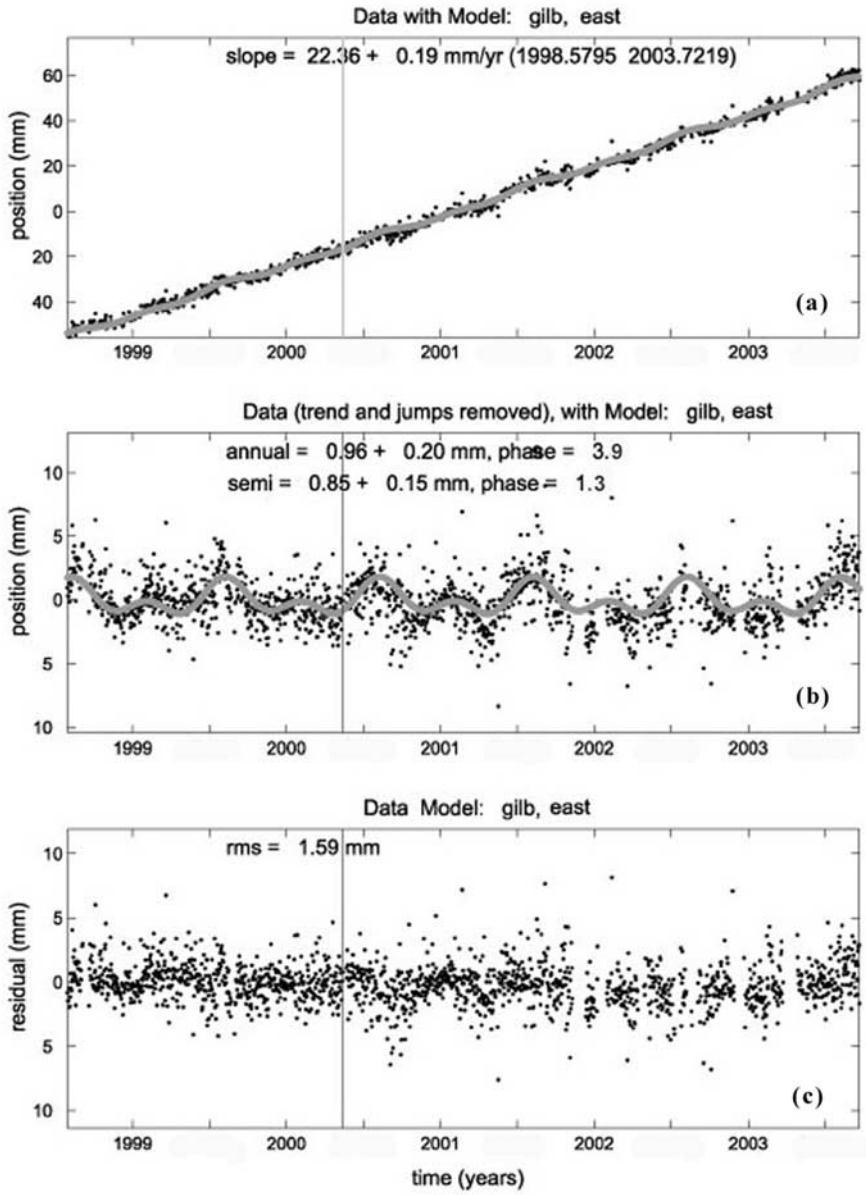

Figure 5. Time series of the GILB east component. (a) Filtered series plotted with secular and seasonal (annual and semi-annual) model (shaded line). (b) Detrended series plotted with annual and semi-annual model parameters. Vertical lines mark the date of antenna change that offsets the series by 1 mm. (c) Residual time series. The reported uncertainties are for the 1-σ level, considering a combined white and flicker noise distribution [*Zhang et al.*, 1997; *Nikolaidis*, 2002].

with the secular as the dominant one. Similarly, the vertical series also represent a superposition of the two patterns, but with a dominant seasonal pattern. In order to quantify the secular and seasonal changes, we apply a multiparameter best fit inversion procedure developed by *Nikolaidis* [2002]. The procedure assumes that the observed motion of each site in each component behaves as a superposition of three processes: a long-term secular change, a cyclic (sinusoidal) annual change, and a cyclic (also sinusoidal) semi-annual change. In addition, the procedure also calculates and corrects offsets caused by equipment replacement.

[15] We demonstrate the fit of this multiparameter model with the GILB East component time series (Figure 5). Although the series is dominated by the secular term, Figure 5b also indicates a significant seasonal term. The residual time series (Figure 5c) provides a good estimate of the noise level (RMS), and a basis for conducting a spatial filtering analysis [*Wdowinski et al.*, 1997]. We apply the multiparameter best fit inversion analyses to the time series (Figure 4) in order to estimate the secular and seasonal terms with lower uncertainties. The results of the best fit analyses are presented in Tables 2, 3, and 4; the reported uncertainties

Table 2. Calculated Station Velocities (Slope) With Respect to ITRF2000* With 1-σ Uncertainties (mm/yr) Assuming White and Flicker Noise Distribution[a]

	North		East		Up	
Site	Slope	1-σ	Slope	1-σ	Slope	1-σ
AMMN	15.16	0.25	22.38	0.28	−2.61	0.79
BSHM	18.44	0.25	22.11	0.26	0.85	1.03
DRAG	18.35	0.23	22.77	0.11	2.63	0.26
ELAT	19.25	0.12	24.91	0.21	−0.80	0.45
ELRO	20.51	0.13	23.05	0.18	0.68	0.61
GILB	19.39	0.11	22.36	0.19	−0.34	0.45
JSLM	18.01	0.10	23.38	0.15	na[b]	
KABR	18.87	0.08	22.02	0.19	−2.01	0.41
KATZ	21.30	0.19	22.23	0.28	2.82	0.68
LHAV	17.89	0.11	22.48	0.31	1.38	0.81
RAMO	18.00	0.36	22.84	0.65	0.66	0.77
TELA	18.54	0.11	23.42	0.21	0.64	0.51
UDMC	21.90	0.11	22.95	0.41	na[b]	

[a][*Zhang et al.*, 1997; *Nikolaidis*, 2002].
[b]The vertical component cannot be resolved accurately enough due to the shortness of the time series and is not used in this study.

assume white and flicker noise distribution [*Zhang et al.*, 1997; *Nikolaidis*, 2002].

5. Current Crustal Movements in the Southern Levant

[16] Our analysis yields quantitative estimates of both secular and seasonal position changes with time (Tables 2, 3, and 4). The secular variations represent steady motion attributed to tectonic (plate motion and crustal deformation) and other long-term processes. The seasonal variations are due to annual and semi-annual atmospheric, oceanic, and hydrological loading [*Dong et al.*, 2002]. We first characterize and evaluate the horizontal secular variations (station velocities) with respect to the tectonic framework of the region. The other observed signals (vertical velocities and seasonal variations) are categorized as non-tectonic movements.

5.1. Current Tectonic Movements: Horizontal Velocities

[17] Table 2 presents the horizontal velocity field of the southern Levant in the ITRF2000* reference frame. It indicates a northeastern movement of all the sites at a rate of 25–30 mm/yr with an uncertainty level of the order 1–2 mm/yr (at 95% confidence level). Because the ITRF2000* is an arbitrary reference frame with no tectonic significance, we need to transfer the observed velocity field into a local tectonically significant reference frame.

[18] We define a Sinai Reference Frame (SRF), which is determined by the velocity vectors of six sites: KABR, BSHM, TELA, JSLM, LHAV, and RAMO (Figure 2). All six sites lie significantly far (more than 30 km, roughly twice the seismogenic depth) from the tectonically active DSF and have long time series. Although KABR lies north of the Carmel Fault (Figure 2), which according to *Salamon et al.* [1996] represents the northern extent of the Sinai subplate, we included KABR in the RF definition because (1) it adds stability and strength for the RF calculations and (2) its horizontal velocity is almost identical to that of BSHM, which is located south of the Carmel Fault. Future studies with denser network across the Carmel Fault will hopefully be able to resolve sub-mm/yr changes across the faults and determine a more accurate Sinai RF.

[19] We use the six velocity vectors to calculate a pole of rotation that minimizes the non-rigid motion between the six sites. Our calculated pole of rotation lies at (53.0°N, 1.7°E) and has an elongated northwest uncertainty direction reflecting the directivity of the velocity field. Because the pole of rotation represents the relative motion of the Sinai block with respect to the arbitrary ITRF2000* reference frame, it has no tectonic significance. We rotate all the velocity vectors about the SRF-ITRF2000* pole to obtain the SRF velocity field (Table 5 and Figure 6).

[20] Figure 6 and Table 5 show that the current relative crustal movements in the southern Levant with respect to the SRF are very slow, 1–4 mm/yr; seven of the nine stations located west of the DSF show no statistically significant motion with respect to the SRF. Two stations located west and adjacent to the DSF (ELAT and GILB) show a small significant northward motion of 0.8–1.0 mm/yr. The four stations located east of the DSF show significant motion with respect to SRF. The three northern stations (KATZ, ELRO, and UDMC) show a northward motion at a rate of 1.7–2.8 mm/yr. This northward motion is consistent with the geologically observed left-lateral movements across the DSF. However, the observed 3.7 mm/yr southward motion

Table 3. Calculated Station Annual Terms: Amplitude (mm), Uncertainty (1-σ White+Flicker Noise) and Phase[a]

	North			East			Up		
Site	Amplitude	1-σ	Phase	Amplitude	1-σ	Phase	Amplitude	1-σ	Phase
AMMN	1.11	0.23	2.694	0.72	0.26	5.089	6.25	0.71	3.216
BSHM	2.38	0.26	0.399	0.95	0.27	0.319	2.50	1.07	3.231
DRAG	0.43	0.20	1.100	0.56	0.15	5.374	5.63	0.36	3.372
ELAT	0.67	0.21	0.763	0.13	0.37	6.216	7.29	0.79	3.029
ELRO	0.83	0.14	6.187	0.15	0.20	0.461	4.64	0.65	3.603
GILB	0.62	0.12	1.592	0.96	0.20	3.890	5.19	0.48	3.262
JSLM	0.51	0.13	0.211	0.89	0.20	4.218	na[b]		
KABR	0.08	0.09	0.706	0.43	0.21	4.374	4.27	0.45	3.167
KATZ	1.72	0.24	0.022	0.17	0.37	4.831	5.22	0.90	3.567
LHAV	1.16	0.10	0.809	0.44	0.28	4.050	4.68	0.74	3.215
RAMO	0.12	0.41	4.791	2.65	0.73	0.191	7.31	0.84	3.090
TELA	0.05	0.15	4.407	0.76	0.28	5.440	6.32	0.67	3.324

[a]Phase represents the radian value (out of 2π periodicity) of the highest amplitude.
[b]The vertical component cannot be resolved accurately enough due to the shortness of the time series and is not used in this study.

Table 4. Calculated Station Semi-Annual Terms: Amplitude (mm), Uncertainty (1-σ White Noise Plus Flicker Noise) and Phase[a]

	North			East			Up		
Site	Amplitude	1-σ	Phase	Amplitude	1-σ	Phase	Amplitude	1-σ	Phase
AMMN	0.32	0.17	1.430	1.19	0.20	0.848	0.78	0.54	0.609
BSHM	0.53	0.19	2.645	0.82	0.20	0.992	0.81	0.79	3.909
DRAG	0.51	0.15	0.728	1.26	0.15	0.880	2.04	0.36	0.971
ELAT	0.70	0.16	2.155	1.16	0.28	1.714	1.24	0.59	0.988
ELRO	0.76	0.10	1.114	0.54	0.15	1.132	0.83	0.49	0.776
GILB	0.75	0.09	1.131	0.84	0.15	1.267	0.92	0.36	6.096
JSLM	0.60	0.13	1.278	0.42	0.20	1.681	na[b]		
KABR	0.60	0.07	1.078	0.60	0.15	1.158	0.19	0.34	1.945
KATZ	0.46	0.18	1.756	0.82	0.27	1.946	1.44	0.66	2.262
LHAV	0.65	0.08	0.975	0.72	0.21	1.528	0.88	0.55	1.533
RAMO	0.52	0.30	1.577	1.13	0.53	0.547	0.63	0.62	1.012
TELA	0.37	0.11	1.483	0.86	0.20	1.683	1.84	0.48	1.111

[a]Phase represents the radian value (out of 2π periodicity) of the highest amplitude.
[b]The vertical component cannot be resolved accurately enough due to the shortness of the time series and is not used in this study.

of AMMN is inconsistent with the tectonic framework of the region.

5.2. Strain Accumulation Across the DSF

[21] In order to evaluate the tectonic significance of the observed velocities, we analyze them with respect to the main tectonic element in the region, the DSF. In this section we ignore the observed motion of AMMN, which indicates a southward motion with respect to Sinai, in contrast to that expected from geological observations. We discuss the AMMN result in the discussion section below.

[22] We evaluate the tectonic significance of the observed velocities using elastic and visco-elastic locked-fault models to demonstrate that our results are valid for more than a single model. Both models calculate the interseismic deformation along active faults, which takes place between major earthquakes. Because the observed east velocities are mostly negligible with respect to their measurement uncertainties, we can ignore their contribution to the models and consider only the north velocities, which represent the fault-parallel component of the north-south oriented DSF. The two northernmost sites, ELRO and UDMC, show a significant eastward motion; we discuss the significance of this motion below. As indicated above, the observed southward motion of AMMN result is inconsistent with left-lateral motion implied by the model (Figure 7) and, hence, cannot be used to constrain the model. UDMC is located significantly far away from the DSF and, hence, its motion with respect to SRF is more representative of the full slip rate along the DSF. The other two eastern stations (ELRO and KATZ) are located very close to the fault (Table 5), within the elastically deforming plate boundary region. Thus their motion reflects only a portion of the full slip rate, roughly two thirds of the total slip rate across the DSF; a detailed analysis of our estimate is given below.

[23] We first present the elastic dislocation model of *Savage and Burford* [1973] for an infinitely long fault. We use this model because it is simple and depends only on three parameters. The model assumes a half space that consists of an upper elastic seismogenic layer of a uniform thickness (D) overlying two blocks sliding horizontally past each other at constant velocity (V_0). The infinitely long fault assumption implies that the velocity of the fault-normal component reduces to zero, whereas the velocity of the fault-parallel component at the surface depends only on the horizontal distance from the fault (x). The mathematical description of the surface fault-parallel velocity is

$$V(x) = V_1 + V_0 \frac{1}{\pi} \arctan\left(\frac{x}{D}\right), \quad (1)$$

where V_1 is an additional nonphysical parameter, representing an arbitrary offset between the velocity profile and the chosen reference frame. Both velocity parameters (V_0 and V_1) are estimated using best fit calculations. The best fit approach for estimating the full plate motion is more robust than the normalized formulation taken by *Pe'eri et al.* [2002], who had only three data points to constrain their model.

[24] We use linear best fit calculations, which allow us to solve for the full plate motion (V_0), but not for the locking depth (D). We apply the model for a range of physically reasonable depths (6–18 km) for strike-slip faults, and based on the nucleation depth of large and moderate earthquakes along the DSF. Below the locking depth, the two elastic blocks are assumed to slide horizontally past each other at constant velocity. Table 6 summarizes our calculations showing our best-estimated slip rate across the DSF and the goodness of fit (χ^2) for all stations and subsets of the stations.

Table 5. Station Velocity as Determined With Respect to SRF With 1-σ Uncertainties (mm/yr) Assuming a White Noise Plus Flicker Noise Model for the Daily Baseline Estimates

	North		East	
Site	Velocity	1-σ	Velocity	1-σ
AMMN	−3.65	0.39	−0.72	0.43
BSHM	0.05	0.29	−0.22	0.46
DRAG	−0.22	0.28	−0.60	0.41
ELAT	0.91	0.19	−0.07	1.18
ELRO	1.75	0.24	0.91	0.59
GILB	0.81	0.22	−0.29	0.37
JSLM	−0.47	0.19	0.18	0.37
KABR	0.39	0.17	−0.14	0.50
KATZ	2.59	0.28	−0.04	0.56
LHAV	−0.43	0.19	−0.98	0.54
RAMO	−0.27	0.40	−1.24	0.98
TELA	0.27	0.21	0.54	0.36
UDMC	2.80	0.31	0.99	0.84

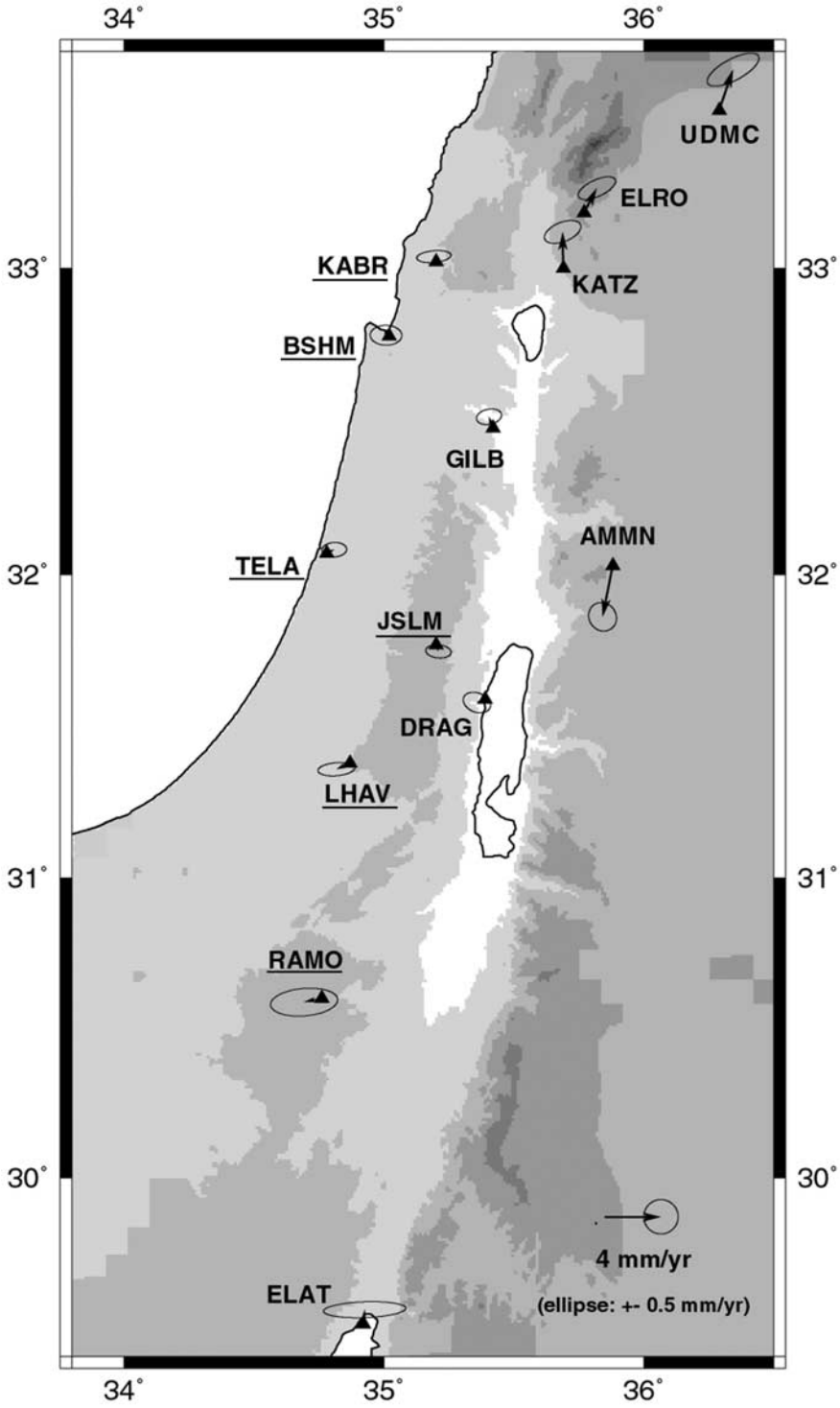

Figure 6. Velocity map of CGPS stations with respect to SRF. Ellipses represent 95% uncertainties estimates, assuming a white noise plus flicker noise model for the position time series. Underlined sites are the reference sites used for defining the Sinai RF.

[25] When using AMMN to constrain the model, we obtain a slow left-lateral motion along the DSF, but with a high χ^2 value. Excluding AMMN from the calculations increases significantly the fit level and generates geologically reasonable results. Our best estimate for the slip rate when using both northern and southern stations is 3.3 ± 0.4 mm/yr (Figure 7). Figure 6 shows that the two northernmost sites, ELRO and UDMC, have significant eastward motion, suggesting that their motion is influenced by change in orientation of the DSF (north of 33.2°) and the compression along Mount Hermon (Figure 1). If we exclude ELRO and UDMC from the model, we obtain a slightly higher slip rate

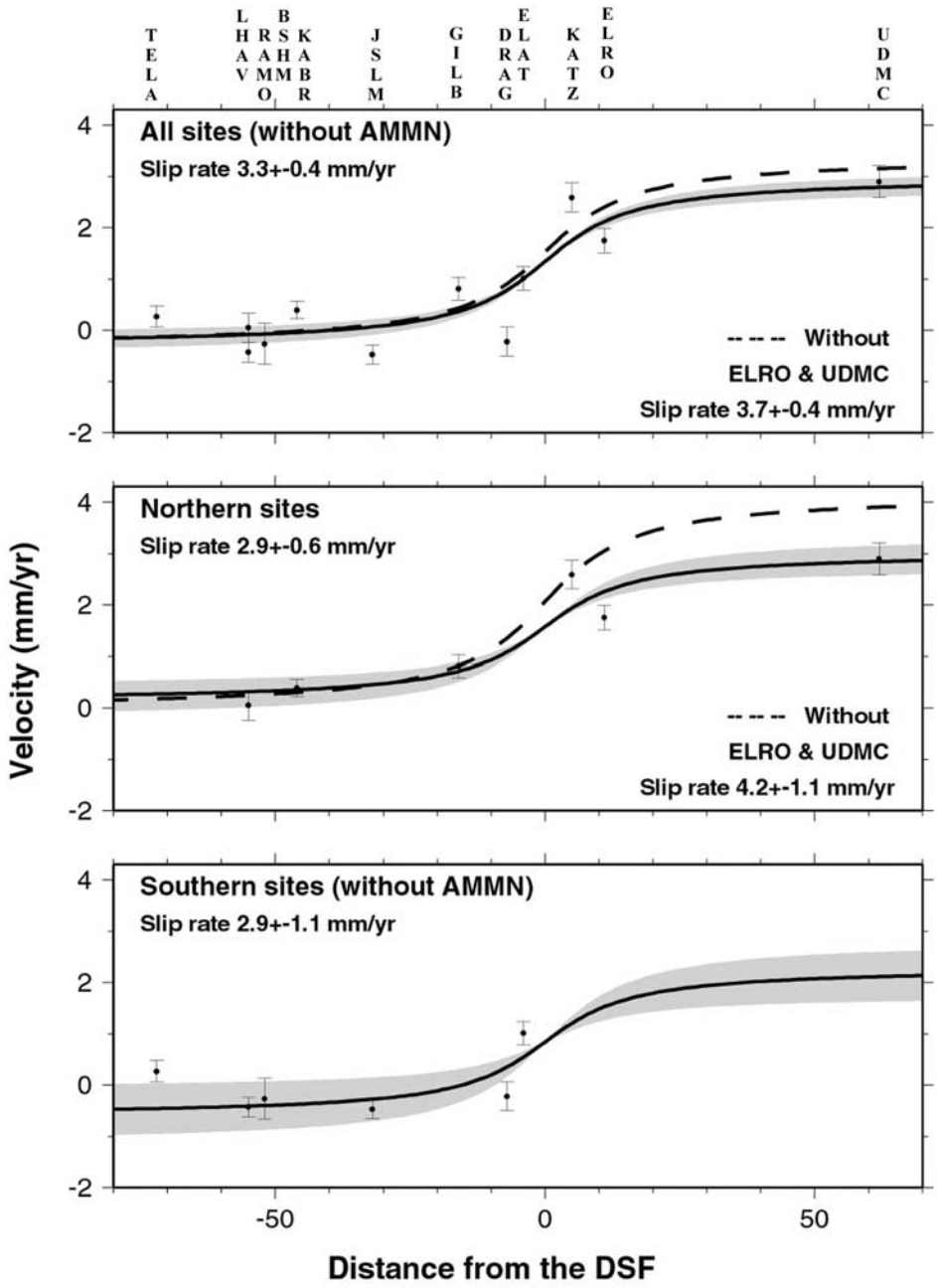

Figure 7. Observed and modeled fault-parallel (V_N) velocity component drawn as function of distance from the DSF for all, northern, and southern sites. The observed velocities are shown with their 1-σ white noise plus flicker noise uncertainties. The modeled velocities are calculated using elastic locked-fault models with 12-km-thick seismogenic layer (*D*). The shaded areas mark the 1-σ uncertainties of the best fit solutions. The negative velocities in the Sinai plate (left of the DSF; Table 5) result from SRF definition, which minimizes the velocity difference between the six reference sites (Figure 6).

of 3.7 ± 0.4 mm/yr; however, this estimate is mathematically less constrained because it relies on a single data point east of the DSF (KATZ).

[26] We also apply the model to two subsets of the northern (BSHM, ELRO, GILB, KABR, KATZ, and UDMC) and southern stations (DRAG, ELAT, JSLM, LHAV, RAMO, and TELA). Applying the model to the northern stations, where we obtain data both east and west of the fault, indicates a slip rate of 2.9 ± 0.6 mm/yr with all sites and 4.2 ± 1.1 mm/yr without ELRO and UDMC. Because the southern stations are located only west of the DSF, the best fit calculations are less constrained, but still indicate a similar slip rate (2.9 ± 1.1 mm/yr) as in the northern stations.

[27] We repeat our calculation using the visco-elastic model of *Savage and Lisowski* [1995] and obtain almost

Table 6. Best Fit Estimates of the Full Plate Motion (V_0) Across the DSF Using an Elastic Dislocation Model With 6-, 12-, and 18-km-Thick Locked Seismogenic Layer (D)[a]

	D = 6 km		D = 12 km		D = 18 km		Weighted Average
	V_0	χ^2_v	V_0	χ^2_v	V_0	χ^2_v	V_0
All sites	1.6 ± 0.1	20.12	1.8 ± 0.1	20.45	2.0 ± 0.1	20.62	1.8 ± 0.3
All except AMMN	2.9 ± 0.1	3.89	3.3 ± 0.1	4.25	3.8 ± 0.1	4.88	3.3 ± 0.4
All except AMMN, ELRO & UMDC	3.6 ± 0.2	3.69	3.8 ± 0.2	4.64	3.8 ± 0.2	5.36	3.7 ± 0.4
Northern sites	2.4 ± 0.1	2.14	2.9 ± 0.1	1.83	3.3 ± 0.6	1.71	2.9 ± 0.6
Northern except ELRO & UDMC	3.3 ± 0.2	0.47	4.2 ± 0.3	0.18	4.8 ± 0.4	0.36	4.2 ± 1.1
Southern sites	−2.8 ± 0.2	10.08	−2.5 ± 0.2	11.71	−2.5 ± 0.2	12.26	−2.7 ± 0.3
Southern except AMMN	3.4 ± 0.7	2.82	2.6 ± 0.5	3.29	2.3 ± 0.5	3.60	2.9 ± 1.1

[a]The reduced-χ^2_v represents the fitness level (lower values reflect better fit). The weighted average gives double weight to the 12-km calculation.

identical results. Because the visco-elastic model depends on more parameters (mantle viscosity, recurrence interval, occurrence of last earthquake), we did not use best fit calculations but instead used simple forward models with the same locking depths and full plate motion as used for the elastic model. The good fit between the two models suggests that mantle-induced deformation is negligible, and that any viscous deformation has relaxed since the last large magnitude earthquake (M > 6) in the northern segment in 1837 [*Marco et al.*, 1997].

[28] In summary, our GPS observations combined with a plate boundary deformation model indicate that the current slip rate across the DSF is 3.3 ± 0.4 mm/yr, but might be slightly higher (3.7 ± 0.4 mm/yr) if ELRO and UDMC are omitted from the calculations, because they are influenced by the compression across Mount Hermon. Dividing the DSF into northern and southern segments suggests that the slip rate across each segment is lower, 2.9 ± 1.1 mm/yr. If we again omit ELRO and UDMC from the calculations, we obtain a higher slip rate across the northern segment (4.2 ± 1.1 mm/yr).

5.3. Nontectonic Movements: Vertical Velocities and Seasonal Variations

[29] The observed vertical velocities are in the range of −2.6 to 2.8 mm/yr and show no regional pattern (Table 2, Figure 2). Out of the 13 GIL/AMMN/UDMC stations, only four stations show statistically significant (above 2-σ) vertical motion (AMMN, DRAG, KABR, KATZ). Two of the stations are subsiding (AMMN and KABR) and two are uplifting (DRAG and KATZ), all in the range of 2–2.8 mm/yr. The geographic location of these four stations (Figure 2) with respect to one another and with respect to the rest of the GIL/AMMN/UDMC stations does not indicate any spatial pattern. Thus we attribute the observed vertical velocities to local processes, such as land sliding, long-term hydrological loading, or monument instability (see discussion).

[30] The observed seasonal variations are most apparent in the vertical component, but can also be seen in the horizontal components. Using *Nikolaidis*' [2002] multiparameter best fit inversion procedure, we estimate annual and semi-annual amplitudes and phases for all time series (Tables 3 and 4). We use the convention of *Nikolaidis* [2002] such that the phase term represents the radian value (out of 2π periodicity) of the highest amplitude. For example, the annual vertical phase of AMMN is 3.216, which represents maximum uplift in the summer (phase ∼ π) and maximum subsidence in the winter. The semi-annual vertical phase of KABR is 3.682, corresponding to maximum uplift in the spring and fall (phase ∼ π) and maximum subsidence in the summer and winter.

[31] Table 3 indicates that the vertical annual component is significant at all stations; however, the horizontal amplitude terms are significant (at 2-σ level) at only half of the stations. The table shows that the annual vertical phase of all stations is similar, occurring over a 35-day period in the summer (days 180–215 corresponding to July–August). In other words, all stations are moving upward from January–February to July–August and downward during the other half of the year. Our vertical phase results (summer uplift) agree well with *Dong et al.* [2002], who conducted a global analysis of CGPS seasonal variations; they show that summer uplift occurs throughout Europe and the Mediterranean regions, but with variable amplitudes. Table 4 shows that the semi-annual component has no outstanding pattern, reflecting local semi-annual movements in all three components.

6. Relative Plate Motion in the Eastern Mediterranean

[32] The Euler pole tying the SRF with the global velocity field also enables us to calculate the relative motion between Sinai and its neighboring plates, as long as their motion are defined in the same reference frame. Although we previously used the ITRF2000* solutions and pole, in this part of our study we prefer using the unfiltered-determined velocity field, which is truly determined in the ITRF2000 reference frame. The difference between the filtered pole (ITRF2000*) and the unfiltered pole (ITRF2000) is small, but important to maintain, due to the high sensitivity of Eulor pole calculations. We also calculated the poles of the neighboring plates, Eurasia (Eu) and Nubia (Nu), but not of Arabia (Ar) due to lack of observations from the Arabian plate (Table 7). In order to overcome this difficulty, we use the ITRF2000 Arabia pole calculated by G. Sella, who updated the REVEL-ITRF97 [*Sella et al.*, 2002] solutions to the currently used ITRF2000 reference frame. We also use the REVEL-ITRF00 poles of Eurasia and Nubia for comparing and complementing our pole calculations.

[33] Obtaining the relative motion between the plates (Table 8) from the list of ITRF2000 poles (Table 7) is straightforward. However, the significance of our results relies on the accuracy of each pole's determination. Unfortunately, the Arabian pole is poorly determined. The REVEL solution for Arabia relies on three velocity vectors. The most reliable one is the velocity of BAHR (Bahrain); the

Table 7. Plate Angular Velocities Relative to ITRF2000 in Geographic Coordinates[a]

Plate	Latitude, °N	Longitude, °E	ω, deg/Myr	σ_{max}[b]	σ_{min}[b]	Azimuth[c]	σω, deg/Myr	Number of Sites	Reference
Si	57.98	−25.11	0.3588	26.59	0.31	−83.8	0.1042	6	this study
Eu	56.70	−100.25	0.2586	0.81	0.19	38.9	0.0016	16	this study
Eu	56.53	−102.49	0.2563	1.4	0.34	32.8	0.0029	15	REVEL-ITRF00
Nu	51.51	−84.04	0.2550	1.44	0.84	−82.2	0.0032	7	this study
Nu	50.14	−78.90	0.2632	1.77	1.03	−85.7	0.0041	5	REVEL-ITRF00
Ar	50.62	2.06	0.5249	3.38	0.72	−72.1	0.0264	3	REVEL-ITRF00

[a]Plate abbreviations: Ar, Arabia; Eu, Eurasia; Nu, Nubia; Si, Sinai. REVEL-ITRF00 is the ITRF2000 update of the REVEL-ITRF97 GPS-determined Euler poles [*Sella et al.*, 2002].
[b]Two-dimensional 1-sigma lengths in degrees of the semi-major σ_{max} and semi-minor σ_{min} of the pole error ellipse.
[c]The azimuth (degrees) is the clockwise angle between north and the semi-major ellipse axis.

other sites are KATZ, which lies in the DSF deformation zone, and the SLR station of Riyadh [*Sella et al.*, 2002]. Alternatively, *McClusky et al.* [2003] used the BAHR and campaign data from three sites located in Turkey about 100–150 km south of the Arabia-Anatolia boundary. Although *McClusky et al.* [2003] did not list their ITRF2000 poles, we added their Eu-Ar pole to our calculated Si-Eu to obtain the Si-Ar pole.

[34] Table 8 shows some differences between the various estimates of the Si-Nu poles, which are all located in a close geographical area. The two poles calculated by this study and the combined solution using the McClusky's Eu-Nu pole are located near the geologically determined Si-Af pole calculated by *Joffe and Garfunkel* [1987]. Whereas the combined solution using the REVEL-ITRF00 Eu-Nu pole is located farther away. All GPS-based estimates of Si-Nu rotation rate are about twice as high as the geological rate of *Joffe and Garfunkel* [1987]. Table 8 also shows some differences between the various estimates of the Si-Ar poles. The poles determined by this study and the combined solution with REVEL-ITRF00 reveal similar locations and rates, because both calculations use the same Ar pole (REVEL-ITRF00). The pole calculated from the combined solution with McClusky's Eu-Ar pole and geologically determined Si-Ar pole of *Joffe and Garfunkel* [1987] are located adjacent to one another. However, the rotation rates of the two solutions are significantly different; the GPS estimated rate is about two thirds of the geological rate.

[35] In order to evaluate the geological significance of the GPS-determined poles, we calculate the predicted motion of each pole along the relevant plate boundary (Table 9). First, we calculate the predicted Si-Ar motion near the Dead Sea (31.5°N, 35.5°E) using both GPS- and geologically-determined poles. Our results show that the GPS-determined relative plate motion between Sinai and Arabia (2.3, 2.6, and 4.3 mm/yr) either underestimate or overestimate our slip-rate estimate along the DSF (3.3 ± 0.4 mm/yr). Both this study and the REVEL-ITRF00 calculations predict a slower rate across the DSF (2.3 and 2.6 mm/yr) directed northwestward, diagonally to the DSF. The predicted northwest motion of Arabia with respect to Sinai indicates a small compressional component (0.8–1.2 mm/yr) across the DSF. Such northwest compression is consistent with the orientation of the Syrian Arc Stress Field [*Letouzey and Tremolieres*, 1980; *Eyal and Reches*, 1983], which has caused compressional deformation in the region since late Senonian (85 Ma) until present [*Eyal*, 1996]. The calculations based on *McClusky et al.*'s [2003] pole predict a higher plate motion rate (4.3 mm/yr) directed northward, parallel to the DSF, similar to direction of motion predicted by the *Joffe and Garfunkel* [1987] pole. The geologically determined motion of *Joffe and Garfunkel* [1987] (6 mm/yr) overestimates the GPS-based relative plate motion estimates, as well as our slip-rate estimates.

[36] We repeat our methodology for evaluating the Si-Nu poles by calculating the motion in the Gulf of Suez (29.0°N, 33.0°E). All solutions indicate extension across the Suez rift, although the direction of motion varies significantly between the various solutions (up to 90° difference). The results show that the predicted rate of motion according to

Table 8. Relative Angular Velocities in Geographic Coordinates[a]

Plate	Latitude, °N	Longitude, °E	ω, deg/Myr	σ_{max}	σ_{min}	Azimuth	σω, deg/Myr	Reference[b]
Si-Eu	23.14	16.62	0.2242	18.12	0.74	58.5	0.1477	this study
Si-Nu	31.04	26.34	0.2029	8.35	1.64	82.5	0.1543	this study
Si-Nu	32.00	32.72	0.1885					$(Si)_{t.s.} + (Ar)_{REVEL}$
Si-Nu	28.60	29.79	0.1861					$(Si)_{t.s.} + (Ar)_{McClusky}$
Si-Af[c]	30.30	28.1	0.093					*Joffe and Garfunkel* [1987]
Si-Ar	−28.71	−150.00	0.2114	6.44	2.49	−60.2	0.1584	$(Si)_{t.s.} + (Ar)_{REVEL}$
Si-Ar	−28.78	−151.39	0.2158					$(Si\text{-}Eu)_{t.s.} + (Eu\text{-}Ar)_{REVEL}$
Si-Ar	−32.76	−159.31	0.1774					$(Si\text{-}Eu)_{t.s.} + (Eu\text{-}Ar)_{McClusky}$
Si-Ar	−32.8	−157.4	0.283					*Joffe and Garfunkel* [1987]
Ar-Eu	−26.03	−157.57	0.4375	2.34	1.11	−76.0	0.0320	REVEL-ITRF00
Ar-Eu	−27.4	−161.6	0.4					*McClusky et al.* [2003]
Eu-Nu	9.71	156.43	0.0698	8.00	4.12	−19.8	0.0055	REVEL-ITRF00
Eu-Nu	0.95	158.2	0.06					*McClusky et al.* [2003]

[a]Columns are the same as in Table 7.
[b]Notations t.s. and REVEL refer to this study and REVEL-ITRF00, respectively.
[c]African plate (Af) was used by *Joffe and Garfunkel* [1987]. More recent studies divide the African plate into Nubian (Nu) and Somalian plates.

Table 9. Calculated Velocities Along the Sinai Plate Boundaries

	Velocity, mm/yr	Azimuth	Reference
		Dead Sea (31.5°N, 35.5°E)	
Si-Ar	2.3	331	$(Si)_{t.s.}$ + $(Ar)_{REVEL}$
Si-Ar	2.6	343	$(Si\text{-}EU)_{t.s.}$ + $(EU\text{-}Ar)_{REVEL}$
Si-Ar	4.3	013	$(Si\text{-}EU)_{t.s.}$ + $(EU\text{-}Ar)_{McClusky}$
Si-Ar	6.0	010	*Joffe and Garfunkel* [1987]
		Suez (29.0°N, 33.0°E)	
Si-Nu	2.4	201	this study
Si-Nu	1.1	265	$(Si\text{-}EU)_{t.s.}$ + $(EU\text{-}Ar)_{REVEL}$
Si-Nu	1.0	173	$(Si\text{-}EU)_{t.s.}$ + $(EU\text{-}Ar)_{McClusky}$
Si-Af	0.8	198	*Joffe and Garfunkel* [1987]

this study's pole is 3 times higher (2.4 mm/yr) than the geological rate (0.8 mm/yr). However, the rate calculated using the REVEL-ITRF00 and *McClusky et al.* [2003] Eu-Nu poles (1.0–1.1 mm/yr) is similar to the geological rate (0.8 mm/yr).

[37] In summary, the GPS-based calculation of the current plate motion in the eastern Mediterranean provides good estimates for plate motion across both the DSF and the Gulf of Suez. Improved estimates of the relative plate motion in the region will become available as the number of reliable GPS sites in the region increases.

7. Discussion

[38] Our analysis of up to 7 years of CGPS data reveals that the current relative crustal movements in the southern Levant with respect to the SRF are very slow, 1–4 mm/yr. The stations located west of the DSF show no significant motion with respect to the SRF, indicating that the entire Sinai block moves as a rigid plate. The four stations located east of the DSF show a significant slow motion with respect to the Sinai block. The three northern stations, which are located in the Golan Heights and Damascus, move northward at a rate of 1.7–2.8 mm/yr. This northward motion is in accordance with the expected left-lateral motion across the DSF. Using locked-fault models, accounting for interseismic strain accumulation along the DSF, and all station velocities except AMMN, we conclude that the current left-lateral slip rate across the DSF is 3.3 ± 0.4 mm/yr. If we further exclude ELRO and UDMC, we derive a rate of 3.7 ± 0.4 mm/yr. Although the slip rate across the northern segment might be slightly higher (4.2 ± 1.1 mm/yr). The observed very small east-west velocity component indicates negligible fault normal movements and deformation. The two sites showing significant eastward motion are ELRO and UDMC, which may reflect compression along the Mount Hermon range.

[39] The previous geodetic estimate of relative plate motion across the DSF was conducted by *Pe'eri et al.* [2002], who used the 3-year-long CGPS data set of the first three sites of the GIL network (ELAT, KATZ, and TELA). They used a similar locked-fault model to estimate the current slip rate at 2.6 ± 1.1 mm/yr, which is slightly lower than our new results based on significantly more data and a more rigorous analysis of the entire network. However, *Pe'eri et al.* [2002] observed 1.7–3.5 mm/yr east-west motion, which is not observed in our new analysis. This significant difference in the east-west motion observed by the two studies arises from the different methodology used by the two studies. *Pe'eri et al.* [2002] used a baseline approach due to their limited number of stations. Although the baseline approach is widely used in local and regional studies, it can propagate reference frame errors. Baseline position changes reflect both deformation and rotation of one site with respect to the other; the rotation component can be eliminated when using baseline lengths rather than baseline vectors. Unaware of the hidden rotation problem, *Pe'eri et al.* [2002] attributed the observed east-west position changes between the three sites to deformation. However, today, we understand that their observed east-west position changes reflect differential rotation rates of the Sinai Block with respect to the ITRF97 reference frame of their analysis and not due to deformation between the sites. The differential rotation problem had a negligible contribution to the north-south component, because the SRF-ITRF pole of rotation lies predominantly northwest of the studied area. In this study we avoided the differential rotation problem by analyzing station positions and rotating the entire velocity field into the SRF.

[40] The relative motion across the DSF has been estimated by a variety of methods. Geological observations, based on processes occurring in the past 25 million years, indicate an average velocity of 6–10 mm/yr [*Quennell*, 1959; *Freund*, 1970; *McKenzie et al.*, 1970; *LePichon and Fancheteau*, 1978; *Ben-Avraham et al.*, 1979; *Garfunkel*, 1981; *Joffe and Garfunkel*, 1987; *Niemi et al.*, 2001]. Geomorphologic observations, based on translocated drainage systems, yield an average velocity of 3–7.5 mm/yr [*Enzel et al.*, 1994; *Ginat et al.*, 1998; *Klinger et al.*, 2000a]. Paleoseismic and historical observations, based on processes occurring in the past thousands to tens of thousands of years, indicate an average velocity of 1.5–3.5 mm/yr [*Ben-Menahem and Aboodi*, 1981; *Shapira and Hofstetter*, 1993; *Klinger et al.*, 2000b]. Seismic observations, based on processes occurring in the past 100 years, indicate an average velocity of 2–4 mm/yr [*Klinger et al.*, 1999; *Salamon et al.*, 2003]. The previous geodetic rate, as determined from 3 years of CGPS data, indicates a relative plate motion of 1.5–3.7 mm/yr [*Pe'eri et al.*, 2002].

[41] Overall, the slip rate across the DSF has been estimated to be in the range of 1–10 mm/yr, depending on the timescale of the observations. Our new estimate of the current slip rate across the DSF, 2.8–3.8 mm/yr and possibly 3.2–4.2 mm/yr (excluding ELRO and UDMC) is higher than the estimate of *Pe'eri et al.* [2002] and is better constrained. Our estimate also overlaps with the 1–4 mm/yr short-term seismic and historic estimates and with the longer-term geomorphologic evidence (3–7 mm/yr). However, it is slower than the geological rates (6–10 mm/yr). Nevertheless, recent geological data from the northern part of the DSF suggest that the geologically derived rate was overestimated by a few tens of percent (Z. Garfunkel, personal communication, 2000). However, published new estimates based on new archeological data suggest still a higher rate [*Meghraoui et al.*, 2003].

[42] The observed southward motion of AMMN disagrees with the expected left-lateral movements across the DSF. The observed steady movement (see continuous time series in Figure 6) represents either a real geophysical movement or an artifact due to monument instability. InSAR analysis of

Amman area shows no detectable movements near the AMMN site during the time span of the GPS observations (1998–2002). However, the very low sensitivity of the InSAR technique to north-south horizontal movements (can detect movements >10 cm) cannot reject or confirm the GPS-observed 4 mm/yr southward movement. Possible movements are land sliding or post-seismic deformation. The AMMN site is located within the RJGC compound on a hilltop composed of stratified limestone. Possibly, the entire hill gravitationally glides along a clay-rich layer. Another possible geophysical explanation, although not very likely, is post-seismic relaxation. AMMN is located about 60 km northeastward of the M = 6.5, 1927 Jericho Earthquake (Figures 1 and 2) and might be subjected to very long-term post-seismic relaxation process. Because two closer sites, DRAG and JSLM, do not show such unusual velocity, we basically rule out the post-seismic mechanism. As mentioned above, the 4 mm/yr southward motion is also accompanied by 2 mm/yr subsidence, and may reflect monument instability. At this stage of the research, we cannot determine the cause for the unexpected AMMN southward motion. Our dependency on one site in Jordan emphasizes the need for further station installations east of the DSF.

8. Conclusions

[43] Seven years of continuous GPS monitoring in the southern Levant provides us with a very accurate description of current crustal movements in the region. The main conclusions of this study are:

[44] 1. The relative station movements in the southern Levant are very small (less than 4 mm/yr).

[45] 2. Most stations (seven out of nine) located west of the DSF show no statistically significant motion with respect to the SRF, suggesting a rigid behavior of the Sinai plate. The observations show no significant movements across the Carmel Fault, which is the second most important fault system in the southern Levant.

[46] 3. The two stations located in the Golan Heights (KATZ and ELRO) and Damascus (UDMC) show 1.7–2.8 mm/yr northward motion with respect to Sinai, indicating a left-lateral motion along the DSF.

[47] 4. Using fault-locked models, we estimate the current slip rate across the DSF at 3.3 ± 0.4 mm/yr. If we exclude ELRO and UDMC, which are located adjacent to the compressional jog of the Mount Hermon range, our estimate increases to 3.7 ± 0.4 mm/yr.

[48] 5. The observed secular vertical movements do not indicate any spatial pattern. We attribute the observed vertical velocities to local processes, such as land sliding, long-term hydrological loading, or monument instability.

[49] 6. Annual seasonal positioning variations are most noticeable in the vertical component. All stations are moving upward from January–February to July–August and downward during the other half of the year.

[50] 7. We calculate the ITRF2000 Sinai pole and use published poles for Arabia, Eurasia, and Nubia to calculate the relative plate motion in the eastern Mediterranean. The GPS-based calculations of the current plate motion provide a good estimate for the Si-Ar motion along the DSF and for the Si-Nu motion across the Gulf of Suez.

[51] **Acknowledgments.** We thank the Royal Jordanian Geographic Center, in particular N. Al-Segerat and G. Ali, for providing us with the AMMN CGPS data. We are grateful to Rob Reilinger for providing the Damascus CGPS data, Amotz Agnon and Xavier Le Pichon, the editor and associate editor, for their helpful reviews, and Giovanni Sella, Rocco Malservisi, and Tim Dixon for their helpful discussions on the relative plate motion and kinematic modeling. We thank Simon McClusky for providing us a pre-print of his paper on plate motions and to the SOPAC staff for their infrastructure support. The figures in this manuscript were produced using the public domain Generic Mapping Tools (GMT) software. The Israel Space Agency and the Survey of Israel funded this study.

References

Adler, R., J. Forrai, and Y. Melzer (2001), The evolution of geodetic-geodynamic control network in Israel, *Isr. J. Earth Sci.*, *50*, 1–7.

Altamimi, Z., P. Sillard, and C. Boucher (2002), ITRF2000: A new release of the International Terrestrial Reference Frame for Earth science application, *J. Geophys. Res.*, *107*, 2214, doi:10.1029/2001JB000561.

Avni, R., D. Bowman, A. Shapira, and A. Nur (2002), Erroneous interpretation of historical documents related to the epicenter of the 1927 Jericho earthquake in the Holy Land, *J. Seismol.*, *6*, 469–476.

Baer, G., D. Sandwell, S. Williams, and Y. Bock (1999), Coseismic deformation associated with the November 1995, Mw = 7.1 Nuweiba earthquake, Gulf of Elat (Aqaba), detected by synthetic aperture radar interferometry, *J. Geophys. Res.*, *104*, 25,221–25,232.

Baer, G., D. Sandwell, G. Shamir, and Y. Bock (2001), Crustal deformation during 6 years spanning the Mw = 7.2 1995 Nuweiba earthquake, analyzed by Interferometric Synthetic Aperture Radar (InSAR), *Isr. J. Earth Sci.*, *50*, 9–22.

Bechor, N. (1998), Tectonic movements in the Sinai Subplate from GPS observations, M.Sc. thesis, Tel Aviv Univ., Tel Aviv, Israel.

Bechor, N., and S. Wdowinski (1998), GPS determined co-seismic displacement induced by the November 1995 Gulf of Elat (Aqaba) earthquake, paper presented at XXVI General Assembly, Eur. Seismol. Comm., Lisbon.

Belitzki, S. (1997), Tectonic geomorphology of the lower Jordan Valley-An active continental rift (in Hebrew with extended English abstract), Ph.D. thesis, 98 pp., Hebrew Univ. of Jerusalem, Jerusalem.

Ben-Avraham, Z., G. Almagor, and Z. Garfunkel (1979), Sediments and structures of the gulf of Elat, *Sediment. Geol.*, *23*, 239–267.

Ben-Menahem, A., and E. Aboodi (1981), Micro- and macroseismicity of the Dead Sea Rift and off-coast eastern Mediterranean, *Tectonophysics*, *80*, 199–233.

Chu, D., and R. G. Gordon (1998), Current plate motions across the Red Sea, *Geophys. J. Int.*, *135*, 313–328.

Dong, D., P. Fang, Y. Bock, M. K. Cheng, and S. Miyazaki (2002), Anatomy of apparent seasonal variations from GPS derived site position time series, *J. Geophys. Res.*, *107*, 2075, doi:10.1029/2001JB000573.

Dubertret, L. (1962), Carte Géologique du Liban, Syrie et bordure de pays voisins, 1:10,00000, Musée d'Hist. Nat., Paris.

Ellenblum, R., S. Marco, A. Agnon, T. Rockwell, and A. Boas (1998), Crusader castle torn apart by earthquake at dawn, 20 May 1202, *Geology*, *26*, 303–306.

Enzel, Y., R. Amit, J. B. J. Harrison, and N. Porat (1994), Morphologic dating of fault scarps and terrace risers in southern Arava, Israel: Comparison to other age dating techniques and implications for paleoseismicity, *Isr. J. Earth Sci.*, *43*, 91–103.

Even-Tzur, G. (2001), Sensitivity analysis of monitoring deformation networks in the north of Israel, *Isr. J. Earth Sci.*, *50*, 23–27.

Eyal, Y. (1996), Stress field fluctuations along the Dead Sea rift since the middle Miocene, *Tectonics*, *15*, 157–170.

Eyal, Y., and Z. Reches (1983), Tectonic analysis of the Dead Sea Rift region since the Late-Cretaceous based on mesostructures, *Tectonics*, 2, 167–185.

Freund, R. (1970), Plate tectonics of the Red Sea and East Africa, *Nature*, *228*, 453.

Freund, R., I. Zak, and Z. Garfunkel (1968), Age and rate of the sinistral movement along the Dead Sea rift, *Nature*, *220*, 253–255.

Freund, R., Z. Garfunkel, I. Zak, M. Goldberg, T. Weisbrod, and B. Derin (1970), The shear along the Dead Sea Rift, *Philos. Trans. R. Soc. London, Ser. A*, *267*, 107–130.

Garfunkel, Z. (1981), Internal structure of the Dead Sea leaky transform (rift) in relation to plate kinematics, *Tectonophysics*, *80*, 81–108.

Garfunkel, Z. (1988), The pre-Quaternary geology of Israel, in *The Zoogeography of Israel*, edited by Y. Yom-Tov and E. W. Tchernov, pp. 7–34, Junk, Hague, Netherlands.

Garfunkel, Z., I. Zak, and R. Freund (1981), Active faulting in the Dead Sea rift, *Tectonophysics*, *80*, 1–26.

Geophysical Institute of Israel (1996), *Seismological Bulletin 1900–1995*, Seismol. Div., Lod, Israel. (Available at http://www.gii.co.il/html/seis/seis_fs.html)

Ginat, H., T. Enzel, and Y. Avni (1998), Translocated Plio-Pleistocene drainage systems along the Arava fault of the Dead Sea transform, *Tectonophysics*, *284*, 151–160.

Heimann, A. (1990), The development of the Dead Sea Transform and its margins in northern Israel during the Pliocene and Pleistocene (in Hebrew with English summary), *Rep. GSI/28/90*, 83 pp., Geol. Surv. of Isr., Jerusalem.

Herring, T. A. (2000), Documentation of the GLOBK Software v. 5.04, report, Mass. Inst. of Technol., Cambridge, Mass.

Hofstetter, A. (2003), Seismic observations of the 22/11/1995 Gulf of Aqaba earthquake sequence, *Tectonophysics*, *369*, 21–36.

Hofstetter, A., H. K. Thio, and G. Shamir (2003), Source mechanism of the 22/11/1995 Gulf of Aqaba earthquake and its aftershock sequence, *J. Seismol.*, *7*, 99–114.

Joffe, S., and Z. Garfunkel (1987), Plate kinematics of the circum Red Sea-A re-evaluation, *Tectonophysics*, *141*, 5–22.

Kimata, F., A. Tealeb, H. Murakami, N. Furukawa, S. Mahmoud, H. Khalil, K. O. Sakr, and A. M. Hamdy (1997), The Aqaba earthquake of November 22, 1995 and co-seismic deformation in Sinai Peninsula deduced from repeated GPS measurements, *Acta Geod. Geophys. Hung.*, *32*(1–2), 53–71.

King, R. W., and Y. Bock (2000), Documentation of the GAMIT GPS Analysis Software v. 9.9, report, Mass. Inst. of Technol., Cambridge, Mass.

Klinger, Y., L. Rivera, H. Haessler, and J. C. Maurin (1999), Active faulting in the Gulf of Aqaba: New knowledge from the M-W 7.3 earthquake of 22 November 1995, *Bull. Seismol. Soc. Am.*, *89*, 1025–1036.

Klinger, Y., J. P. Avouac, N. Abou Karaki, L. Dorbath, D. Bourles, and J. L. Reyss (2000a), Slip rate on the Dead Sea transform fault in northern Araba valley (Jordan), *Geophys. J. Int.*, *142*, 755–768.

Klinger, Y., J. P. Avouac, C. Dorbath, N. Abou Karaki, and N. Tisnerat (2000b), Seismic behavior of the Dead Sea fault along Araba valley, Jordan, *Geophys. J. Int.*, *142*, 769–782.

Knafo, R., and S. Wdowinski (2000), Construction of Global Positioning System (GPS) permanent stations in Israel, *Rep. TR-GSI/12/2000*, pp. 1–7, Geol. Surv. of Isr., Jerusalem.

Le Pichon, X., and J. Francheteau (1978), A plate-tectonic analysis of the Red Sea-Gulf of Aden Area, *Tectonophysics*, *46*, 369–406.

Letouzey, J., and P. Tremolieres (1980), Paleo-stress around the Mediterranean since the Mesozoic from microtectonic: Comparison with plate tectonic data, *Rock Mech.*, *9*, 173–192.

Marco, S., A. Agnon, R. Ellenblum, A. Eidelman, U. Basson, and A. Boas (1997), 817-year-old walls offset sinistrally 2.1 m by the Dead Sea Transform, Israel, *J. Geodyn.*, *24*, 11–20.

McClusky, S., et al. (2000), Global Positioning System constraints on plate kinematics and dynamics in the eastern Mediterranean and Caucasus, *J. Geophys. Res.*, *105*, 5695–5719.

McClusky, S., R. Reilinger, S. Mahmoud, D. Ben Sari, and A. Tealeb (2003), GPS constraints on Africa (Nubia) and Arabia plate motions, *Geophys. J. Int.*, *155*, 126–138.

McKenzie, D., D. Davies, and P. Molnar (1970), Plate tectonics of the Red Sea and East Africa, *Nature*, *226*, 243–248.

Meghraoui, M., et al. (2003), Evidence for 830 years of seismic quiescence from palaeoseismology, archaeoseismology and historical seismicity along the Dead Sea fault in Syria, *Earth Planet. Sci. Lett.*, *210*, 35–52.

Niemi, T. M., et al. (2001), Late Pleistocene and Holocene slip rate of the Northern Wadi Araba fault, Dead Sea Transform, *Jordan J. Seismol.*, *5*, 449–474.

Nikolaidis, R. (2002), Observation of geodetic and seismic deformation with the Global Positioning System, Ph.D. thesis, Scripps Inst. of Oceanogr., La Jolla, Calif.

Ostrovsky, E. (2001), The G1 GPS geodetic-geodynamic reference network: Final processing results, *Isr. J. Earth Sci.*, *50*, 29–37.

Pe'eri, S., S. Wdowinski, A. Shtivelman, N. Bechor, Y. Bock, and M. van Domselaar (2002), Current plate motion across the Dead Sea Fault, as observed from 3 years of continuous GPS monitoring, *Geophys. Res. Lett.*, *29*(14), 1697, doi:10.1029/2001GL013879.

Pinar, A., and N. Turkelli (1997), Source inversion of the 1993 and 1995 Gulf of Aqaba earthquakes, *Tectonophysics*, *283*, 279–288.

Quennell, A. M. (1958), The structural and geomorphic evolution of the Dead Sea rift, *Q. J. Geol. Soc. London, Part 1*, *114*, 1–24.

Quennell, A. M. (1959), Tectonics of the Dead Sea rift, *Int. Geol. Congr., 20th, Mexico, 1956- Assoc. Serv. Geol. Afr.*, 385–405.

Salamon, A. (1993), Seismotectonic analysis of earthquakes in Israel and adjacent Areas, Ph.D. thesis, Hebrew Univ., Jerusalem.

Salamon, A., A. Hofstetter, Z. Garfunkel, and H. Ron (1996), Seismicity of the eastern Mediterranean region: Perspective from the Sinai subplate, *Tectonophysics*, *263*, 293–305.

Salamon, A., A. Hofstetter, Z. Garfunkel, and H. Ron (2003), Seismotectonics of the Sinai subplate-The eastern Mediterranean region, *Geophys. J. Int.*, *155*, 149–173.

Savage, J. C., and R. O. Burford (1973), Geodetic determination of relative plate motion in central California, *J. Geophys. Res.*, *78*, 832–845.

Savage, J. C., and M. Lisowski (1995), Strain accumulation in Owens Valley, *Seismol. Soc. Am. Bull.*, *85*, 151–158.

Sella, G. F., T. H. Dixon, and A. Mao (2002), REVEL: A model for Recent plate velocities from space geodesy, *J. Geophys. Res.*, *107*, 2081, doi:10.1029/2000JB000033.

Shamir, G. (1996), The November 22, 1995, Nuweiba Earthquake, Gulf of Elat (Aqaba): Mechanical analysis, *Rep. 550/87/96*, Geophys. Inst. of Isr., Lod, Israel.

Shamir, G., G. Baer, and A. Hofstetter (2003), Three-dimensional elastic earthquake modelling based on integrated seismological and InSAR data: The M-w = 7.2 Nuweiba earthquake, gulf of Elat/Aqaba 1995 November, *Geophys. J. Int.*, *154*, 731–744.

Shapira, A., and H. Hofstetter (1993), Source parameters and scaling relationships of earthquakes in Israel, *Tectonophysics*, *217*, 217–226.

Smith, D. E., R. Kolenkiewicz, J. W. Robbins, P. J. Dunn, and M. H. Torrence (1994), Horizontal crustal motion in the central and eastern Mediterranean inferred from satellite laser ranging measurements, *Geophys. Res. Lett.*, *21*, 1979–1982.

Wdowinski, S., Y. Bock, J. Zhang, and P. Fang (1997), Southern California Permanent GPS Geodetic Array: Spatial filtering of daily positions for estimating coseismic and postseismic displacements induced by the 1992 Landers earthquake, *J. Geophys. Res.*, *102*, 18,057–18,070.

Wdowinski, S., Y. Bock, Y. Forrai, Y. Melzer, E. Ostrovsky, G. Baer, and D. Levitte (2001), The GIL network of continuous GPS monitoring in Israel for geodetic and geophysical applications, *Isr. J. Earth Sci.*, *50*, 39–47.

Wilson, J. T. (1965), A new class of faults and their bearing on the continental drift, *Nature*, *207*, 343–347.

Zhang, J., Y. Bock, H. Johnson, P. Fang, S. Wdowinski, J. Genrich, and J. Behr (1997), Southern California Permanent GPS geodetic array: Error analysis of daily position estimates and site velocities, *J. Geophys. Res.*, *102*, 18,035–18,056.

G. Baer and R. Knafo, Geological Survey of Israel, 30 Malkhe Yisrael St., Jerusalem, 95501, Israel. (baer@mail.gsi.gov.il)

N. Bechor and S. Naaman, Department of Geophysics and Planetary Sciences, Raymond and Beverly Sackler Faculty of Exact Sciences, Tel Aviv University, Ramat Aviv 61390, Israel. (nbechor@stanford.edu)

Y. Bock and L. Prawirodirdjo, Cecil H. and Ida M. Green Institute of Geophysics and Planetary Physics, Scripps Institution of Oceanography, La Jolla, CA 92093-0225, USA. (ybock@igpp.ucsd.edu; linette@ucsd.edu)

Y. Forrai and Y. Melzer, Survey of Israel, 1 Lincoln St., Tel Aviv, 65220, Israel. (forrai@mapi.gov.il; yml@soi.gov.il)

S. Wdowinski, Division of Marine Geology and Geophysics, Rosenstiel School of Marine and Atmospheric Science, University of Miami, 4600 Rickenbacker Causeway, Miami, FL 33149-1098, USA. (shimonw@rsmas.miami.edu)